Turbine power loss during yaw-misaligned free field tests at different atmospheric conditions

Paul Hulsman[1], Carlo Sucameli[2], Vlaho Petrović[1], Andreas Rott[1], Alexander Gerds[3] and Martin Kühn[1]

[1] ForWind – Center for Wind Energy Research, Institute of Physics, University of Oldenburg, Küpkersweg 70, 26129 Oldenburg, Germany
[2] Wind Energy Institute, Technical University of Munich, 85748 Garching b. München, Germany
[3] Eno energy systems GmbH, Kempowski-Ufer 1, 18055 Rostock

E-mail: `paul.hulsman1@uol.de`

Abstract. This paper presents an analysis of the power loss of the upstream turbine for yaw misalignment depending on the inflow condition. High-quality experimental field data, obtained from a lidar wind profiler, met mast, GPS based yaw sensor, turbine data, and load data is used. To reduce the spreading of the power loss during yaw misalignment, the rotor effective wind speed is estimated using load data. Furthermore, the so-called power loss coefficient currently used in most engineering models, for yaw misalignment, is assessed at various inflow conditions. As main finding, the power loss coefficient increases for stronger vertical wind shear. In addition, there is an asymmetry with respect to the direction of the yaw misalignment that is enhanced by the wind shear exponent and the wind veer. Neglecting these two effects could result in in-conservative wake-steering decisions at stable stratification.

1. Introduction

Redirecting the wake of the upstream turbine away from the downstream turbine by yawing is regarded as a promising approach to increase the overall power output of a wind farm as it was indicated in simulations [1, 2], wind tunnel experiments [3, 4, 5], and field experiments [6, 7, 8, 9].

Currently, yaw controllers are developed using engineering models [10, 11] to determine the optimal yaw angle for maximising the power output. A major factor affecting the efficiency of wake steering is the power loss of the upstream turbine with regard to the yaw misalignment angle (ψ). Within most engineering models, the power output is modelled as $P = P_0 \cos^p(\psi)$, where p is the power loss coefficient and P_0 is the power of the turbine aligned with the wind.

Based on the elementary Blade Element Momentum theory, the power loss coefficient should be $p = 3$. However, multiple values for the power loss coefficient have been presented in literature and vary significantly depending on turbine model and

experimental setup. [2] used a value of $p = 1.88$ which was determined using SOWFA simulations with the NREL 5MW turbine. [6] found a value of $p = 1.4$ for the Envision 4MW turbine using LES and experimental data. [12] also observed a similar value for the Vestas V27 using LES ($p = 1.4$). During wind tunnel experiments, [13, 3] measured a value of $p \approx 2$ and [4] determined a value of $p \approx 3$ with a different model turbine. [14] reported a range of $p \in [1.88, 5.14]$ at an offshore demonstration facility.

Further investigation indicated that the power loss coefficient differs for waked turbines and depends on the yaw misalignment of the upstream turbine [15]. [16] determined using LES that the coefficient for the downstream turbine lies within $p \in [1.3, 2.5]$. Recent research [17] revealed that the power loss coefficient differs at different wind speed regions due to the changed thrust coefficient. [18] found an asymmetry in the power loss depending on the yaw direction. The analysis indicated higher losses occurred for a clockwise rotation caused by the rotation direction of the rotor and the incoming wind speed and direction profiles.

The significant variation of the values presented in literature and its dependency on the inflow condition show that an accurate estimate of the power loss coefficient is lacking and that a model is necessary for the development of a yaw controller as it could lead to unfavourable wake steering scenarios.

The aim of this paper is to quantify the effect of the shear, veer, and turbulence intensity on the power loss of the upstream turbine using comprehensive free field measurement data. Knowing the relation between the power loss coefficient and the inflow condition, the effect of the various inflow conditions on the power loss coefficient is then presented. This will indicate whether a fixed power loss coefficient is suitable to accurately estimate the power loss of the misaligned turbine. The gained insight will help to determine whether the development of a simplified analytical model is needed. Such a model could be implemented into existing wake steering models to estimate the power loss and improve the determination of the optimal yaw angle.

2. Methodology
At first the setup and layout of the experimental campaign used to obtain the power output of the upstream turbine during yaw misalignment is described. This is followed by the method used to accurately assess the lidar wind profiler measurements. Through the use of the rotor effective wind speed, obtained by the lidar measurements, the averaged thrust and power coefficient were determined. Subsequently, to reduce the present scatter in the field data the thrust coefficient is used to determine the rotor effective wind speed from the load measurements. Lastly, numerical simulations were performed at different inflow conditions to validate the observations in the free field.

2.1. Field campaign
Free field measurement data has been gathered from an experimental campaign conducted from the end of December 2020 to the beginning of July 2021 at an onshore wind farm with two 3.5 MW wind turbines in Kirch Mulsow, north-eastern Germany, as a cooperation of eno energy systems, ForWind, and TU Munich. The turbines have a distance of 2.7 diameter ($D = 126\,\mathrm{m}$), as illustrated in Figure 1 (right), with a hub height (h) of $117\,\mathrm{m}$ (WT1) and $137\,\mathrm{m}$ (WT2) respectively. With a wind direction (θ_{WD})
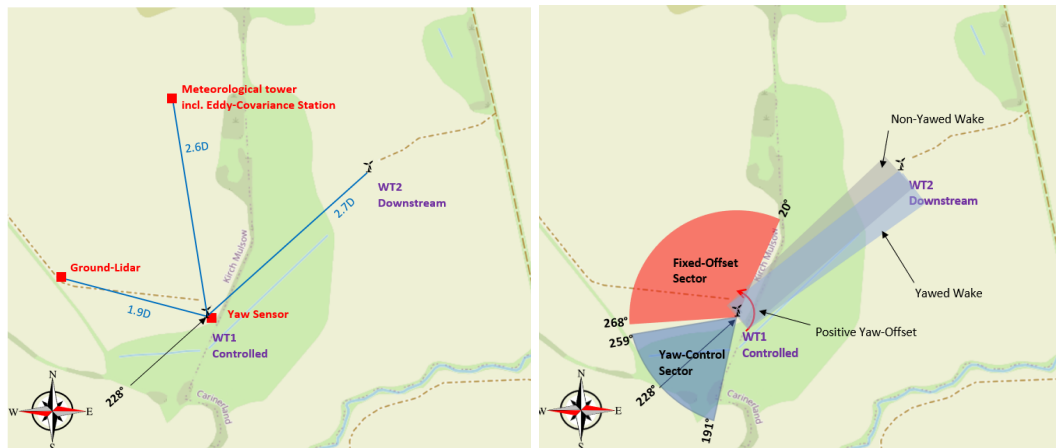
Figure 1: **Left:** Layout of the experimental field campaign. The position of both turbines, the met mast, and the lidar wind profiler are shown. The upstream turbine (WT1) and the downstream turbine (WT2) was equipped with a GPS based yaw sensor. **Right:** Illustration of the two wind sectors. The "yaw control sector" was used to test different controllers. In the "fixed-offset sector" a target offset of $\pm 15°$ was applied.

of $228°$, the two WTs are oriented in the flow direction, with WT1 being the upstream turbine. Since this corresponds to the main wind direction, WT1 was selected for the testing of yaw controllers. In order to determine the 'true' yaw offset, both WTs were additionally equipped with GPS based yaw sensors.

To acquire more information on the incoming wind condition, such as wind speed profiles and wind direction profiles, a lidar wind profiler was installed at a distance of $1.9\,D$ from WT1. Throughout the entire field campaign, the lidar performed a velocity azimuth display (VAD) scan gathering wind speeds on a vertical cone with an elevation angle of $75°$ and a scanning speed of $30°/s$. Furthermore, a met mast (MM) located $2.6\,D$ from WT1 was also used to measure the inflow condition at a sampling rate of $50\,Hz$. It was equipped with cup anemometers and wind vanes at $54\,m$ and $112\,m$. At $110\,m$, the temperature and the pressure was recorded at the same frequency. Additionally, three Eddy-Covariance Stations were installed at a height of $2\,m$, $6\,m$ and $54\,m$ to determine the atmospheric stratification averaged over $30\,minutes$.

As this campaign was also used to evaluate different control strategies, two separate wind sectors were used and defined as the "yaw control sector" and the "fixed-offset sector", as shown in Figure 1. In the "yaw control" sector ($[191°, 259°]$), two distinct yaw controllers were used, which were developed by ForWind and the TU Munich, respectively. They were activated and compared to the greedy-controller (normal operation). The two yaw controllers and the greedy controller (normal operation) were sequentially toggled every $35\,minutes$, which generated a database with various yaw misalignments. As the name suggests, in the second sector ($[268°, 360°] \cup [0°, 20°]$) a commanded fixed offset ($\pm 15°$) was used to characterise the turbine performance during yaw misalignment. Similar to the first sector, the offset was toggled every $35\,minutes$ between $+15°$, $-15°$ and the greedy-controller. Due to the continuous change of the yaw

misalignment, 60s averaged quantity are analysed. SCADA data, including signals such as turbine power, turbine heading, and turbine status were stored at a sampling rate of 50 Hz. During this analysis, the data acquired in both sectors are used to characterise the performance of the upstream turbine depending on the yaw misalignment.

2.2. Lidar wind profiler

The lidar wind profiler was performing a VAD scan every 12 s to capture the inflow condition over the entire rotor area. From each lidar scan, θ_{WD} and horizontal wind speed is determined at the heights $h \in \{48\,\mathrm{m}, 53\,\mathrm{m}, \ldots, 188\,\mathrm{m}\}$ using a cosine fit to detect the azimuth angle of the lidar beam with the largest radial wind speed.

To identify possible effects due to the induction zone of the turbine, the mean ratio of the averaged horizontal wind speed component of the lidar U_{VAD}, and the wind speed measured by the met mast at hub height U_{MM} is illustrated in Figure 2. Here, U_{VAD} is defined as the averaged horizontal wind speed component with the azimuth angle θ_{WD} at a distance of at least $2.14\,D$. The data was averaged to 60s values and the wind direction bin width is $10°$. The total number of 60s averaged quantities in this experiment was 29386 while the turbine was operational. The data used for this analysis includes shear exponent $\alpha \in [-0.05, 0.5]$, veer angle $\theta_{\mathrm{veer}} \in [-10°, 10°]$, $U_{\mathrm{MM}} \in [4\,\mathrm{m/s}, 10\,\mathrm{m/s}]$ and TI $< 15\%$. In the non-waked section (shaded green) the ratio was ≈ 1 within $\theta_{\mathrm{WD}} \in [191°, 270°]$, after which it increases to ≈ 1.05 until a wind direction of $\approx 50°$. This can be due to the presence of high trees in front of the met mast, which causes a 'peak' of 1.09 at the wind direction $350°$ when the met mast was aligned to the upstream turbine.
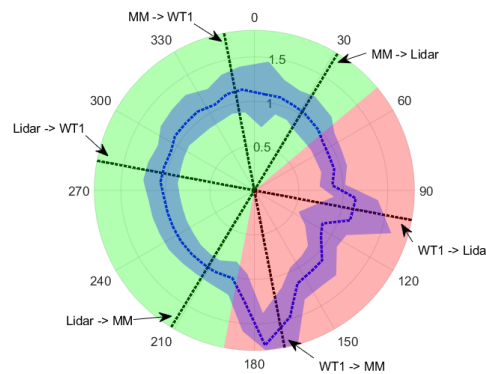

Figure 2: The blue dotted line indicates the averaged ratio $U_{\mathrm{VAD}}/U_{\mathrm{MM}}$ of 60s averaged quantities within a wind direction bin width of $10°$. The blue shaded area highlights $\pm \sigma$. The black dotted lines mark θ_{WD} when either the met mast (MM), WT1 or the lidar are aligned. The red area illustrates the waked section and the green area the non-waked section. The arrows show equipment located upstream and downstream.

2.3. Rotor effective wind speed (REWS)

The use of point measurements at hub height from the met mast resulted in a large scatter of the power coefficient due to the frequent presence of large shear and veer. The application of the REWS measured by the lidar also resulted in a large scatter, as the wind field measured at $2.14\,D$ was disturbed due to the shear, veer, and turbulence when reaching the rotor. In addition, the available data set would be significantly reduced when using the lidar wind profiler as it was not always operational. Since the loads were measured throughout the entire campaign, the REWS was estimated using the averaged measured thrust coefficient during non-misaligned cases ($|\psi| < 2.5°$). A first order approximation was used to estimate the thrust from the tower bottom bending moment measured by strain gauges. This was achieved by subtracting the tower bottom bending moments due to the weight of the rotor and nacelle ($M_{x,0}$, $M_{y,0}$), determined at stand still, from the overall bending moment (M_x, M_y). The effect of the rotor torque on the side-to-side tower bottom bending moment was neglected. The non-misaligned thrust T_{ref} was obtained using Equation 1 and subsequently used to compute the non-misaligned thrust coefficient $c_{T_{\mathrm{ref}}}$, see Equation 2. This was done using the instantaneous air density ρ, the rotor area A and the REWS ($U_{\mathrm{eff,VAD}}$) measured by the lidar with a wind direction ranging from $191°$ to $300°$ where $U_{\mathrm{VAD}}/U_{\mathrm{MM}} \approx 1$. Here h_T equals the hub height minus the height of the strain gauge position.

$$T_{\mathrm{ref}} = \sqrt{\left(\frac{M_{\mathrm{x,Tower}} - M_{\mathrm{x,0}}}{h_T}\right)^2 + \left(\frac{M_{\mathrm{y,Tower}} - M_{\mathrm{y,0}}}{h_T}\right)^2} \tag{1}$$
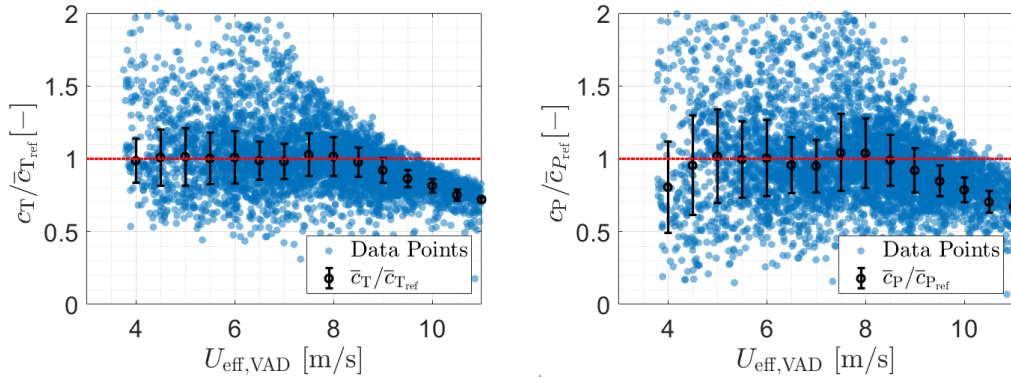

Figure 3: Thrust (**Left**) and power coefficient (**Right**), normalised with the averaged value of the corresponding coefficient without yaw misalignment between $4.75\,\mathrm{m/s}$ and $8.75\,\mathrm{m/s}$, $\overline{c}_{T_{\mathrm{ref}}}$ and $\overline{c}_{P_{\mathrm{ref}}}$, with regard to $U_{\mathrm{eff,VAD}}$. The black dots indicate the averaged normalised coefficients for $U_{\mathrm{eff,VAD}}$ within the wind speed bins $\{3.75\,\mathrm{m/s}, 4.25\,\mathrm{m/s}, \ldots, 11.25\,\mathrm{m/s}\}$ with the corresponding error bar ($\pm\sigma$). The red line illustrates the reference at 1

$$c_{T_{ref}} = \frac{T_{ref}}{0.5\rho U_{eff,VAD}^2 A} \qquad (2)$$

The normalised thrust coefficient without yaw misalignment is depicted in Figure 3, where the maximum thrust coefficient was obtained below 8.75 m/s. The wind speed region with the maximum power coefficient ranges between 4.75 m/s and 8.75 m/s, which is used during further analysis and to determine the averaged thrust $\bar{c}_{T,ref}$ and power $\bar{c}_{P,ref}$ coefficient. The coefficients are normalised using the corresponding averaged value without yaw misalignment within the selected wind speed range. To estimate the REWS during a 'true' yaw misalignment ($\psi = \theta_{Met} - \theta_{GPS}$), from the thrust coefficient, it needs to be corrected for different yaw misalignment values using the relation in Equation 3.

$$c_{T_\psi} = \bar{c}_{T_{ref}} \cos(\psi) \qquad (3)$$

Figure 4 presents the fitted cosine function using a least square fit and a bootstrapping method with 1000 iterations and a 95 % confidence interval. During each iteration, the coefficient q is determined with the least square method with the function $c_T = \bar{c}_{T_{ref}} \cos^q(\psi)$ using randomly selected data samples from the the filtered data. The randomly selected data samples equals the size of the filtered data and hence duplicate samples are included during the fitting. This results in a data series of 1000 coefficients based on which the mean q_0 and the standard deviation σ_q can be derived to indicate the spread of the coefficient $q = q_0 + \sigma_q$. For each yaw bin $\{-32.5°, -28.5°, \ldots, 32.5°\}$ with more than 30 data samples (30 times 60s averaged quantity resulting in 30 min), a boxplot is included indicating the median (central mark), the 25th percentile (bottom
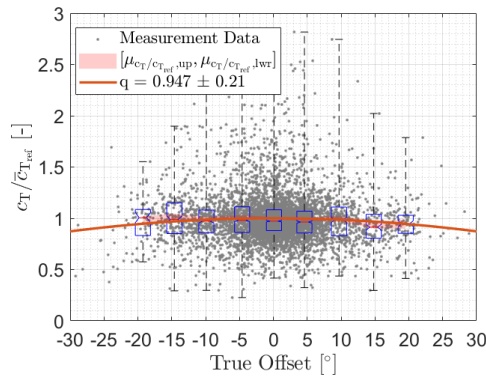

Figure 4: Normalised c_T with regard to the yaw misalignment with $\alpha \in [-0.05, 0.5]$, $\theta_{veer} \in [-10°, 10°]$, $U_{eff,VAD} \in [4.75 m/s, 8.75 m/s]$ and TI < 7.5 %. The coefficient is normalised with the averaged value with no yaw misalignment between 4.75 m/s and 8.75 m/s. The grey dots represent the 60s averaged quantities. The box plot indicate the quartiles within each yaw bin $\{-32.5°, -28.5°, \ldots, 32.5°\}$. The red shaded area indicates the upper (maximum) and lower bounds (minimum) using a bootstrapping method. The solid red line shows the cosine fit with the mean coefficient q_0 ($q = q_0 \pm \sigma_q$)
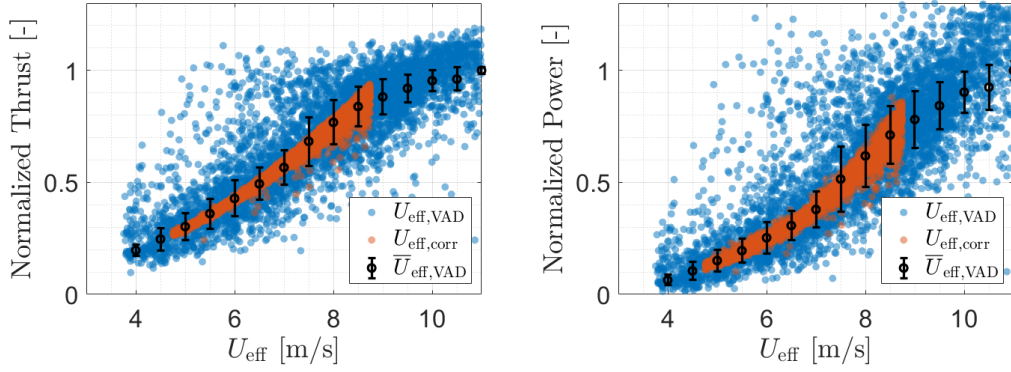
Figure 5: Normalised 60s averaged thrust (**Left**) and power (**Right**) with regard to $U_{\mathrm{eff,VAD}}$ $\{3.75\,\mathrm{m/s}, 4.25\,\mathrm{m/s}, \ldots, 11.25\,\mathrm{m/s}\}$ (blue dots) and $U_{\mathrm{eff,corr}} \in [4.75\mathrm{m/s}, 8.75\mathrm{m/s}]$ (red dots) respectively. The thrust T_{ref} and the power P are normalised by the averaged value with no yaw misalignment between $10.75\,\mathrm{m/s}$ and $11.75\,\mathrm{m/s}$. The blue dots represent the 60s averaged quantities. The black dots indicate the average of the blue dots and the error bar $(\pm\sigma)$ for each wind speed bin

mark) and the 75th percentile (top mark). The data used for this analysis includes $\alpha \in [-0.05, 0.5]$, $\theta_{\mathrm{veer}} \in [-10°, 10°]$, TI $< 7.5\,\%$ and $U_{\mathrm{eff,corr}} \in [4.75\,\mathrm{m/s}, 8.75\,\mathrm{m/s}]$, where c_{P} and c_{T} remain constant. A value of $q = 0.95 \pm 0.21$ is found when fitting over the entire data set, confirming $c_{\mathrm{T}_\psi} = \bar{c}_{\mathrm{T}_{\mathrm{ref}}} \cos(\psi)$. By using this relation for the thrust coefficient, the corrected REWS ($U_{\mathrm{eff,corr}}$) seen by the rotor can be determined.

$$U_{\mathrm{eff,corr}} = \sqrt{\frac{T_\psi}{0.5\rho A \bar{c}_{\mathrm{T}_{\mathrm{ref}}} \cos(\psi)}} \tag{4}$$

The reduction of the scatter on the thrust and the power is visible in Figure 5, where the measured power and thrust component is plotted against $U_{\mathrm{eff,corr}}$ and $U_{\mathrm{eff,VAD}}$. Besides reducing the scatter, the corrected REWS is related to the turbine position and, thus, minimising any effects due to the terrain on the met mast and lidar. $U_{\mathrm{eff,corr}}$ is eventually used to compute the power coefficient c_{P} using Equation 5 and the measured power P. As the met mast data are further used in combination with the load measurements to increase the data availability, the following definitions are used: $\theta_{\mathrm{veer}} = \theta_{\mathrm{WD,hh}} - \theta_{\mathrm{WD,hlwr}}$, and $\alpha = \log(U_{\mathrm{hlwr}}/U_{\mathrm{hh}})/\log(54/112)$, where 'hlwr' indicates the lower tip height at $54\,\mathrm{m}$ and 'hh' indicates the measurements at $112\,\mathrm{m}$.

$$c_{\mathrm{P}} = \frac{P}{0.5\rho U_{\mathrm{eff,corr}}^3 A} \tag{5}$$

2.4. Numerical Simulation

Two high fidelity simulations with different inflow conditions were performed to verify the observed dependency of the power loss to the inflow condition in the free field measurement data. Both simulations were performed using PArallelised Large

eddy simulation Model (PALM) [19] revision model 3193, which uses non-hydrostatic incompressible Boussinesq approximation of the Navier-Stokes equations. The Monin-Obukhov Similarity Theory was used to exchange information between the surface and the lowest grid cell. The generated wind fields are used as an input to the aeroelastic tool FAST v8 [20], where a calibrated model of the reference turbine was used. Both cases have a duration of $5400\,\text{s}$, while using a roughness length of $0.1\,\text{m}$ and a grid spacing $\Delta = 5\,m$. The boundary conditions include: 'Neumann' at the surface, 'radiation' at the outlet and 'Dirichlet' at the inlet. The first simulation was performed with a grid size of $511\,\text{m}\,\text{x}\,96\,\text{m}\,\text{x}\,2047\,\text{m}$, while using turbulent recycling at a distance of $2000\,\text{m}$ from the inlet, where the the precursor simulation was introduced into the main simulation. Here, a surface temperature of $280\,\text{K}$ and a temperature gradient of $1\,\text{K}/100\,\text{m}$ starting at $100\,\text{m}$ was applied. Using the same definition used for the free field measurement data, this resulted to the inflow parameters $\alpha = 0.46$, $\theta_{\text{veer}} = 16.88°$, $U_{\text{hh}} = 7.17\text{m/s}$, and TI $= 6.99\,\%$. The second simulation was performed with a grid size of $511\,\text{m}\,\text{x}\,160\,\text{m}\,\text{x}\,2047\,\text{m}$ and a turbulent recycling distance of $5500\,\text{m}$. A surface temperature of $283.15\,\text{K}$ was used with a temperature gradient of $8\,\text{K}/100\,\text{m}$ starting at $500\,\text{m}$ up to $600\,\text{m}$, where a temperature gradient of $1\,\text{K}/100\,\text{m}$ sets off. This leads to the inflow parameters $\alpha = 0.28$, $\theta_{\text{veer}} = 3.74°$, $U_{\text{hh}} = 7.90\text{m/s}$, and TI $= 6.66\,\%$. For the analysis the flow fields from PALM with the time periods $[3000\,\text{s}, 4200\,\text{s}]$, $[3600\,\text{s}, 4800\,\text{s}]$, and $[4200\,\text{s}, 5400\,\text{s}]$ was coupled to FAST simulations at $\psi = \{-40°, -30°, ..., 40°\}$ resulting in $2\,\text{x}\,9$ simulations. The time periods overlap, to omit the first $600\,\text{s}$ to account for the transient period within FAST. The resulting power data was further discretised to obtain the 60s averaged c_{P} with the corresponding yaw misalignment.

3. Results and discussion

The power with respect to the yaw misalignment is presented in Figure 6 for three different shear exponent (α) ranges: a) $[-0.1, 0.1]$ c) $[0.1, 0.3]$ e) $[0.3, 0.5]$ with $\theta_{\text{veer}} \in [-10°, 10°]$, $U_{\text{eff,corr}} \in [4.75\,\text{m/s}, 8.75\,\text{m/s}]$, and TI $< 7.5\%$. This means that only data points (60s averaged quantities) are included when the turbine was in Region II and the blades were not pitching. Moreover, data points including active yaw manoeuvres were omitted and the power coefficient was normalised with the averaged power coefficient within its respective wind speed bin of $\{4.75\,\text{m/s}, 5.25\,\text{m/s}, \ldots, 8.75\,\text{m/s}\}$. This resulted in 1120 (Figure 6a), 2492 (Figure 6c) and 2547 (Figure 6e) data points for the three different shear exponent ranges. Here the same approach was applied to determine the power loss coefficient p carried out for the thrust coefficient in subsection 2.3, except that the transformation $c_{\text{P}} = c_{\text{P}_0} \cos^p(\psi)$ was used. Here c_{P_0} is the averaged power coefficient determined using $U_{\text{eff,corr}}$ with no yaw misalignment for each separate inflow case. The shaded red area presents the upper and lower bound of the mean normalised power coefficient for each yaw bin using again a bootstrapping method to determine the mean value with a confidence interval of 95% with 1000 iterations. The upper and lower bound indicate the maximum and minimum mean value obtained within all iterations.

　Figure 6a illustrates a power loss coefficient of $p = 2.13 \pm 0.11$ at $\alpha \in [-0.1, 0.1]$ which increases to $p = 2.26 \pm 0.09$ at $\alpha \in [0.1, 0.3]$ (Figure 6c). The highest power loss coefficient is seen at the highest shear range in Figure 6e with $p = 2.54 \pm 0.12$. This suggests that the power loss coefficient is dependent on the shear exponent. A higher loss
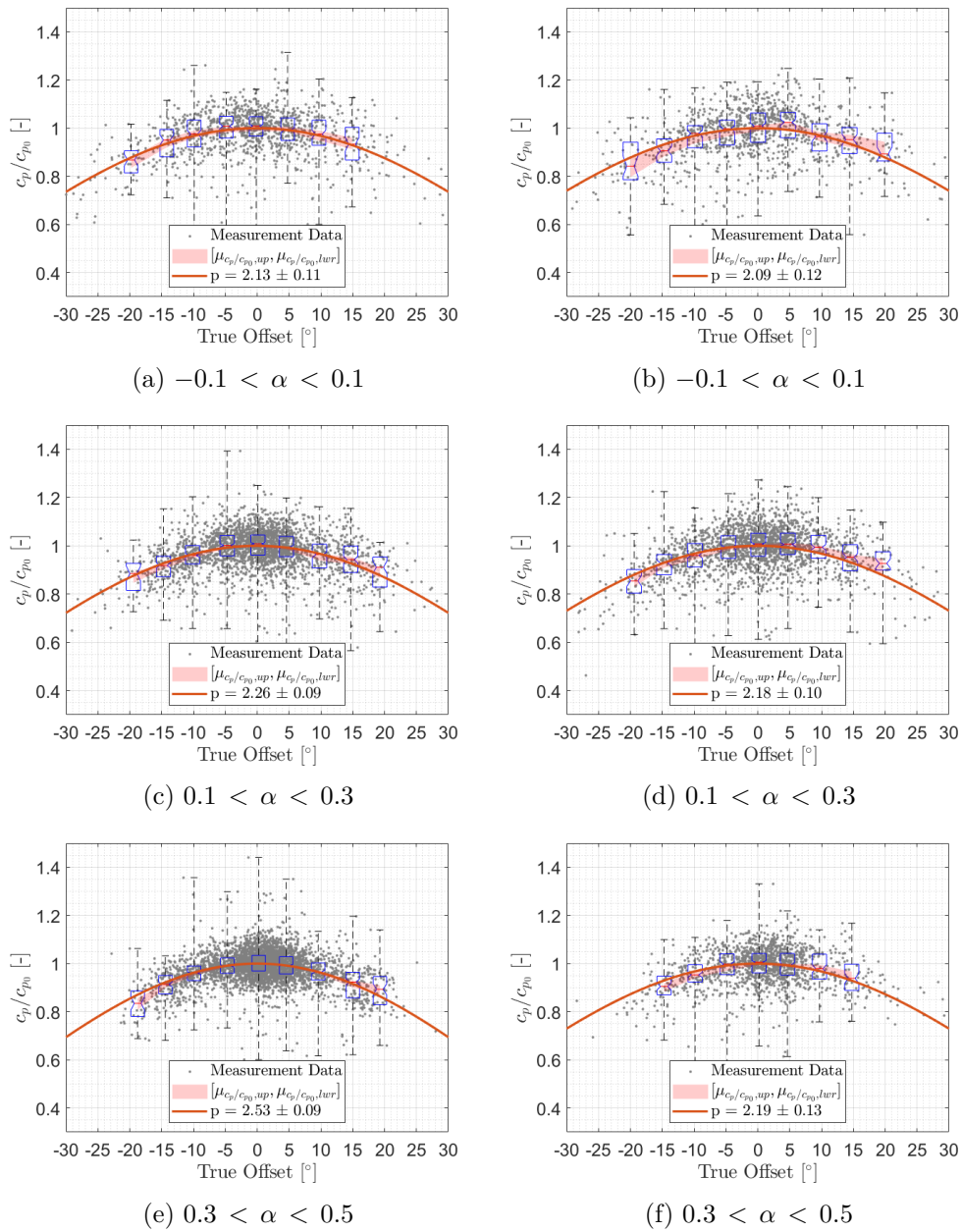
Figure 6: **a, c, e:** Mean power loss coefficient p_0 is shown for three different shear cases with $\theta_{veer} \in [-10°, 10°]$, $U_{\text{eff,corr}} \in [4.75\text{m/s}, 8.75\text{m/s}]$ and TI $< 7.5\,\%$. **b, d, f:** with TI $\in [7.5\%, 15\%]$. The grey dots represent the 60s averaged quantities. The box plot indicate the quartiles within each yaw bin of $\{-32.5°, -28.5°, \ldots, 32.5°\}$. The red shaded area indicates the upper (maximum) and lower bounds (minimum) using a bootstrapping method. The solid red line indicates the cosine fit with p_0 ($p = p_0 \pm \sigma_p$)
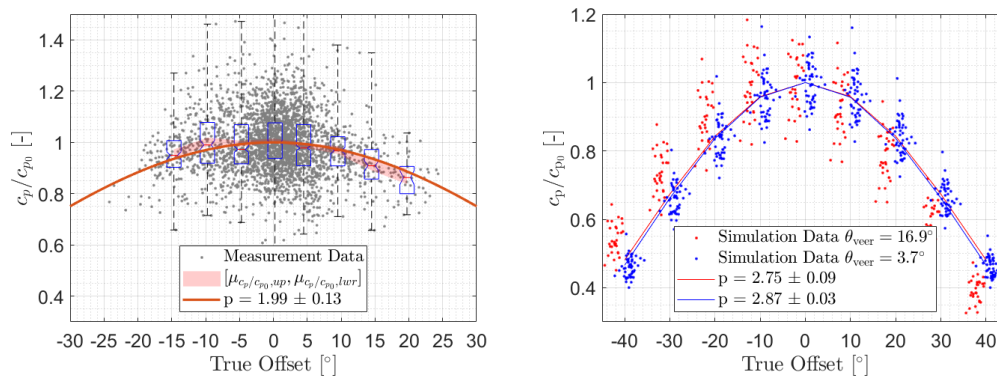
Figure 7: **Left:** Power loss coefficient from field data is shown for a case with $\alpha \in [0.3, 0.5]$, $\theta_{\text{veer}} \in [10°, 30°]$, $U_{\text{eff,corr}} \in [4.75\,\text{m/s}, 8.75\,\text{m/s}]$, and TI $< 7.5\,\%$. The grey dots represent the 60s averaged quantities. The box plot indicate the quartiles within each yaw bin of $\{-32.5°, -28.5°, \dots, 32.5°\}$. The red shaded area indicates the upper (maximum) and lower (minimum) using a bootstrapping method. The solid red line indicates the cosine fit with the mean coefficient p_0 ($p = p_0 \pm \sigma_p$) **Right:** Numerical simulations performed with PALM and FAST v8 for two different inflow conditions including the cosine fit for each case

is experienced when yawing the turbine with increasing shear. It is observed that a higher shear exponent occurs more frequently at very stable atmospheric conditions, where the turbulent production is suppressed leading to a low wind direction variability and, thus, to a larger impact due to yaw misalignment. Furthermore, at a large shear exponent, the surplus of the available power above the hub height is higher than the reduction of the available power below the hub height. This can point to a larger relative power loss on an outboard blade segment. This would signify that the behaviour of the power loss during yaw misalignment related to the shear exponent is linked to the turbine design, as it depends on the lift distribution over the blade.

The same procedure is applied with the data points with the turbulence intensity between 7.5 % and 15 % for each shear case resulting in 1521 (Figure 6b), 2659 (Figure 6d) and 1884 (Figure 6f) number of 60s averaged quantities. Here, the power curve is more 'flattened' out leading to a power loss coefficient 2.09 ± 0.12, 2.18 ± 0.10, and 2.19 ± 0.13 respectively. A higher turbulence intensity indicates a higher wind direction variability and, as such, reduces the impact of a yaw misalignment on the power production. This is because the upstream turbine is not always aligned to the incoming wind direction at a higher wind direction variability. Furthermore, the effect of an increasing power loss coefficient is not detected with a higher turbulence intensity range.

Besides the increase of the power loss coefficient, a minor asymmetry of the normalised power coefficient is visible between a positive and a negative yaw misalignment. Figure 6a to Figure 6e show a slightly larger median of the power coefficient for $\psi \in [17.5°, 22.5°]$ in comparison to the negative yaw bins, which seems to increase at a larger shear.

However, the difference lies within the uncertainty of the measurements. An even higher asymmetry is observed in Figure 7, when filtering the data with $\alpha \in [0.3, 0.5]$, $\theta_{\text{veer}} \in [10°, 30°]$, $U_{\text{eff,corr}} \in [4.75\text{m/s}, 8.75\text{m/s}]$, and TI $< 7.5\,\%$. Within the larger veer angle range it was observed that the assumption of using Equation 3 was not valid and that the thrust with regard to yaw does not follow a cosine-like behaviour. Therefore, the met mast wind speed is used to compute the power coefficient. During this case a ratio of $c_{P,\psi \in [17.5, 22.5]}/c_{P,\psi \in [-22.5, -17.5]} = 0.92$ is observed. This asymmetry was also described in [21] and in [18]. Figure 6 and Figure 7 highlight that the interaction of the rotation of the blades, the incoming wind profile and the crosswind component present during yaw misalignment causes the asymmetry in the power loss. In this case, the crossflow component due to a large positive wind veer enhanced the asymmetry.

The same effect of the asymmetry in the power loss is clearly visible (Figure 7) in the numerical simulations due to the presence of a large positive wind veer. For the numerical case with $\theta_{\text{veer}} = 16.9°$ with $p = 2.75 \pm 0.09$ a higher power output is simulated at $\psi < 0°$ in comparison to $\psi > 0°$. This asymmetry is not visible for the numerical case with $\theta_{\text{veer}} = 3.7°$, where the coefficient $p = 2.87 \pm 0.03$ matches the simulations points very well. Figure 7 (Right) emphasises the shortcomings of using a cosine function to capture the turbine loss, as it does not account for an asymmetric behaviour. A higher power loss coefficient is obtained with the numerical simulation, which can be related to the reduced dynamic wind direction changes in comparison to the free field data.

The results indicate that atmospheric stability strongly correlates with the coefficient p. Stable atmospheric stratification, which is more suitable for wake deflection (see [22]), results in a larger power loss coefficient at higher shear, which means that the upstream wind turbine suffers more losses due to yaw misalignment. A coefficient of $p = 2.13$ gives a power loss of approximately $7.2\,\%$ for a yaw misalignment of $15°$ for the upstream wind turbine. In comparison, a coefficient of $p = 2.53$ causes a power loss of $8.4\,\%$. Hence, assuming a too low value of p would be in-conservative. The presence of veer could be favourable for wake steering as the power loss is reduced for a positive yaw angle. However, at a negative yaw angle a larger power loss is present. Successful wake control must ensure that these losses are exceeded by increased power at the downstream WT.

4. Conclusion

Based on the field data an increase of the power loss coefficient for yaw misalignment is observed with larger shear exponents. This can be due to the atmospheric stratification as large shear angles occur more frequently at stable conditions, where the turbulence is suppressed and, hence, leads to a low wind direction variability. Another possible explanation is the interaction of the wind speed profile and the power loss at each blade segment during yaw misalignment. At a higher turbulence intensity, the power loss curve is 'flattened', due to the higher wind direction variability. Furthermore, an asymmetry of the power loss is observed between a positive yaw misalignment and a negative yaw misalignment. It is found that a minor asymmetry increases with an increasing shear, but is mostly impacted in the presence of large veer angles. The asymmetry is related to the interaction between the rotation of the blade and the crosswind component present during yaw misalignment and at large veer angles. The same trend related to the veer angle is also observed during the comparison with Large Eddy Simulations. The

dependency of the power loss coefficient with regard to the inflow conditions indicate that the commonly used approach, assuming a constant value to estimate the power loss is insufficient. To take these effects into account, it is imperative to develop a simplified model or a modification to the current approach for wind farm control based on wake steering. The model can then be incorporated within existing wake steering models to improve the determination of the optimal yaw angle.

Acknowledgments

References

[1] Fleming P, Gebraad P M, Lee S, van Wingerden J W, Johnson K, Churchfield M, Michalakes J, Spalart P and Moriarty P 2015 Wind Energy **18**(12) 2135–2143
[2] Gebraad P, Thomas J J, Ning A, Fleming P and Dykes K 2017 Wind Energy **20**(1) 97–107
[3] Medici D 2005 Experimental studies of wind turbine wakes: power optimisation and meandering Ph.D. thesis KTH
[4] Bartl J, Mühle F, Schottler J, Sætran L, Peinke J, Adaramola M and Hölling M 2018 Wind Energy Science **3**(1) 329–343
[5] Hulsman P, Wosnik M, Petrović V, Hölling M and Kühn M 2022 Wind Energy Science **7**(1) 237–257
[6] Fleming P, Annoni J, Shah J J, Wang L, Ananthan S, Zhang Z, Hutchings K, Wang P, Chen W and Chen L 2017 Wind Energy Science **2**(1) 229–239
[7] Howland M F, Lele S K and Dabiri J O 2019 Proceedings of the National Academy of Sciences **116**(29) 14495–14500
[8] Fleming P, King J, Dykes K, Simley E, Roadman J, Scholbrock A, Murphy P, Lundquist J K, Moriarty P, Fleming K et al. 2019 Wind Energy Science **4**(2) 273–285
[9] Fleming P, King J, Simley E, Roadman J, Scholbrock A, Murphy P, Lundquist J K, Moriarty P, Fleming K, van Dam J et al. 2020 Wind Energy Science **5**(3) 945–958
[10] Bastankhah M and Porté-Agel F 2014 Renewable Energy **70** 116–123
[11] Martínez-Tossas L A, Annoni J, Fleming P A and Churchfield M J 2019 Wind Energy Science **4**(1) 127–138
[12] Hulsman P, Andersen S J and Göçmen T 2020 Wind Energy Science **5**(1) 309–329
[13] Madsen H A, Sørensen N N and Schreck S 2003 Wind Energy Symposium **75944** 94–103
[14] Dahlberg J and Montgomerie B 2005 Research program of the utgrunden demonstration offshore wind farm, final report part 2, wake effects and other loads Tech. Rep. 02-17 Swedish Defense Research Agency (FOI), Kista, Sweden
[15] Liew J, Urbán A M and Andersen S J 2020 Wind Energy Science **5**(1) 427–437
[16] Draper M, Guggeri A, López B, Díaz A, Campagnolo F and Usera G 2018 Journal of Physics: Conference Series **1037** 072051
[17] Simley E, Fleming P, Girard N, Alloin L, Godefroy E and Duc T 2021 Wind Energy Science **6**(6) 1427–1453
[18] Howland M F, González C M, Martínez J J P, Quesada J B, Larranaga F P, Yadav N K, Chawla J S and Dabiri J O 2020 Journal of Renewable and Sustainable Energy **12**(6) 063307
[19] Maronga B, Gryschka M, Heinze R, Hoffmann F, Kanani-Sühring F, Keck M, Ketelsen K, Letzel M O, Sühring M and Raasch S 2015 Geoscientific Model Development **8** 2515–2551
[20] Jonkman J M, Buhl Jr M L et al. 2005 National Renewable Energy Laboratory, Golden, CO, Technical Report No. NREL/EL-500-38230
[21] Doekemeijer B M, Kern S, Maturu S, Kanev S, Salbert B, Schreiber J, Campagnolo F, Bottasso C L, Schuler S, Wilts F et al. 2021 Wind Energy Science **6**(1) 159–176
[22] Vollmer L, Steinfeld G, Heinemann D and Kühn M 2016 Wind Energy Science **1**(2) 129–141